

Fast, accurate, and predictive method for atom detection in site-resolved images of microtrap arrays

Marc Cheneau,* Romaric Journet, Matthieu Boffety, François Goudail, and Caroline Kulcsár
*Université Paris-Saclay, Institut d’Optique Graduate School,
CNRS, Laboratoire Charles Fabry, 91127, Palaiseau, France*

Pauline Trouvé-Peloux
DTIS, ONERA, Université Paris-Saclay, 91123, Palaiseau, France
(Dated: February 13, 2025)

We introduce a new method, rooted in estimation theory, to detect the individual atoms in site-resolved images of microtrap arrays, such as optical lattices or optical tweezer arrays. Using simulated images, we demonstrate a ten-fold reduction of the detection error rate compared to the popular method based on Wiener deconvolution, under a wide range of experimental conditions. The runtime is fully compatible with real-time applications, even for a very large arrays. Finally, we propose a rigorous definition for the signal-to-noise ratio of an image, and show that it can be used as a predictor for the detection error rate, which opens new prospect for the design of future experiments.

I. INTRODUCTION

Over the past 15 years, site-resolved imaging of atoms or molecules in arrays of optical microtraps, whether optical lattices or optical tweezer arrays, has been established as a sensitive probe of spatial correlations in a quantum many-body system [1, 2]. In a typical experimental setting, a two-dimensional array loaded with atoms, with an inter-site distance ranging from a few hundred nm to a few μm , is imaged onto a digital camera with a high-resolution objective. After calibration of the coordinates of the sites in the image and the profile of the point spread function (PSF) of the optical system, the image is then processed to detect the presence or absence of an atom in each site. The reconstruction of the site occupancies is therefore a classical estimation-detection problem [3, 4], where the signal to be estimated consists in the brightness of each site.

When the inter-sites distant is larger than the optical resolution, a simple binning approach is often sufficient to estimate the site brightnesses [5–8]. Otherwise, one has to resort to more elaborate estimation techniques. The methods employed so far can be broadly categorized as local non-linear least squares [9–12], local iterative algorithms [13, 14], deconvolution methods [15–22], local maximum likelihood estimation [23, 24] and supervised [25, 26] or unsupervised [27] neural networks. Recently, the performance of several methods, among which the popular Wiener and Richardson-Lucy deconvolution methods, has been compared using labelled test images simulating an optical tweezer array experiment [28]. A non-linear least squares approach was shown to achieve the best accuracy, but at the cost of a prohibitive computation time.

In this article, we apply a generalized Wiener filter [3]—which uses the statistical properties of both the signal and the noise to provide an optimal linear estimate of the signal—to the reconstruction of the site occupancies. We focus on the more difficult problem posed by optical lattices, where neighboring sites often have a significant overlap, but the method equally applies to any type of microtrap array. Using labelled test images, we compare the performance of our method with that of the Wiener deconvolution, and demonstrate a ten-fold reduction of the detection error rate under a wide range of experimental conditions. Importantly, we achieve this result with low computation times, well below 100 ms for 100×100 sites. We also keep the implementation simple by using the Python interpreted programming language and standard scientific computing libraries, and provide the reader with a tutorial example in the form of a Jupyter notebook [29].

Last but not least, our approach provides a rigorous definition of a signal-to-noise ratio for the reconstruction problem, i.e. a synthetic indicator of the intrinsic ‘difficulty’ of the estimation-detection problem under given experimental conditions. We show that this indicator can be used as a predictor for the detection error rate. This predictor should greatly improve the design of new experimental apparatuses because it allows one to establish clear specifications for the imaging system, rather than simply maximizing the optical resolution and the number of photons emitted by the atoms, as was done until now. One can then take advantage of the improved accuracy of our method to either lower the requirements on the imaging system, or reduce the inter-site distance to increase the coupling between sites and access new physics, for instance.

* marc.cheneau@institutoptique.fr

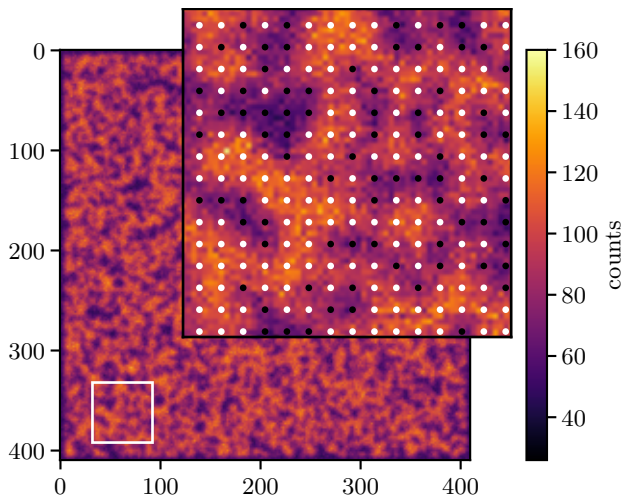


FIG. 1. **A randomly generated test image.** The image mimics an optical lattice configuration. The imaging parameters are listed in Table I. They were chosen on purpose to make the reconstruction problem difficult, but still tractable. The inset shows a zoom into the white square towards the bottom left corner of the image, with the white and black dots indicating, respectively, the occupied and empty sites. Our reconstruction method detects the atoms in this image with an error rate of 0.19%, compared to 1.35% with a deconvolution estimator.

number of sites	N_s	100×100	
occupancy probability	p	0.6	
lattice spacing	a	4	pixel
PSF HWHM		3	pixel
brightness mean	μ	1000	count / site
brightness variance	σ^2	100	count / site
background	k	50	count / pixel
readout noise variance	r^2	1	count / pixel

TABLE I. **Imaging parameters for Fig. 1.** The unit of length is set by the pixel size. An Airy disk with the same half width at half maximum (HWHM) as our Gaussian PSF would have its radius (first zero) at approximately $2.4 \times 3/4 \simeq 1.8 a$. With such a large radius, none of the usual resolution criteria is met.

II. METHODOLOGY

To quantitatively evaluate and compare the performance of different reconstruction algorithms, we generate random test images using an idealized model [30]. We define a square lattice with N_s sites in an image with N_p pixels, and denote a the lattice spacing in the image plane (measured in pixels). The top left site is centered on a pixel unless a global offset is applied to the site positions. The occupancy of each site is drawn randomly from a Bernoulli distribution with the occupancy probability p . The brightness of the empty sites is taken to be zero, while that of the occupied site follows a normal distribution with its mean and variance denoted, respec-

tively, by μ and σ^2 . Once the brightnesses have been chosen, we build a noiseless image by summing the PSF of each site multiplied by the corresponding brightness, and adding a uniform background k (the camera readout offset is taken to be zero for simplicity). Finally, we obtain the test image by treating each pixel of the noiseless image as the mean value of a Poisson distribution—which accounts for the shot noise—and then adding a normally distributed noise with zero mean and variance r^2 —which accounts for the readout noise of a CMOS camera. In the following we designate the model parameters introduced above as the *imaging parameters*, since all but the occupancy probability characterize the imaging system or the imaging process.

The relationship between the site brightnesses and the pixel values in the test image can be summarized in the following matrix equation:

$$\mathbf{y} \sim \mathcal{P}(\mathbf{M}\mathbf{x} + \mathbf{k}) + \mathcal{N}(\mathbf{0}, \mathbf{r}^2). \quad (1)$$

Here, and in the following, small bold letters denote column vectors, capital bold letters matrices, and (small or capital) normal letters scalars. The vector \mathbf{y} represents the pixel values, \mathbf{x} the brightnesses, $\mathbf{k} = k\mathbf{1}$ the background, and $\mathbf{r}^2 = r^2\mathbf{1}$ the readout noise. \mathbf{M} is the measurement matrix, with $(\mathbf{M})_{ij}$ the integral over the i th pixel of the PSF centered on the j th site. $\mathcal{P}(\mathbf{u})$ and $\mathcal{N}(\mathbf{u}, \mathbf{v})$ denote, respectively, the multivariate Poisson distribution with mean \mathbf{u} , and for the multivariate normal distribution with mean \mathbf{u} and diagonal covariance matrix $\text{diag}(\mathbf{v})$. $\mathbf{1}$ and $\mathbf{0}$ denote the column vectors of ones and zeros.

We have chosen a Gaussian PSF, characterized by its half width at half maximum (HWHM), and normalized such that its area integral is equal to unity (i.e. $\sum_i (\mathbf{M})_{ij} = 1$). The PSF is truncated when the distance to the center is larger than 3 times the HWHM. The reader accustomed to modelling the PSF by an Airy disk can convert the Gaussian HWHM to the radius of the Airy disk by multiplying the former with a factor 2.4 (assuming that both functions have the same HWHM).

We show in Fig. 1 one example of a test image, mimicking an optical lattice configuration, which we will use throughout the article to illustrate our method. The corresponding imaging parameters, given in Table I, were chosen such that the reconstruction is barely possible using conventional techniques. In particular, the PSF HWHM is too large (with respect to a) for any of the usual resolution criteria to be met.

Denoting $\hat{\mathbf{x}}$ the estimated brightnesses (i.e. the output of an estimation algorithm), we quantify the estimation accuracy through the sum of squared residuals:

$$\text{SSR} \triangleq \|\hat{\mathbf{x}} - \mathbf{x}\|_2^2. \quad (2)$$

A site is labelled as occupied if its estimated brightness lies above a global detection threshold. We quantify the detection accuracy through the detection error rate:

$$\text{DER} \triangleq \frac{\text{FP} + \text{FN}}{N_s}, \quad (3)$$

where FP and FN stand for the number of false positives and false negatives, and the terms ‘positives’ and ‘negatives’ refer to sites labelled as occupied or empty, respectively. Since we know the ground truth behind the test images, we simply choose the detection threshold which minimizes the DER.

III. OPTIMAL LINEAR ESTIMATOR

We now turn to the description of our approach to solve the estimation problem. It starts with the choice of a model for the relationship between the measurement (\mathbf{y}) and the signal (\mathbf{x}):

$$\mathbf{y} = \mathbf{M}\mathbf{x} + \mathbf{k} + \mathbf{n} . \quad (4)$$

Here, \mathbf{y} , \mathbf{x} , \mathbf{k} and \mathbf{M} have the same meaning as in Eq. (1). The vector \mathbf{n} accounts for the shot noise (originating from both the atomic and background signals) and for the camera readout noise. This model is relevant in most experimental contexts, and exact for our test images, because it is always possible to split a random vector with a Poisson statistics in its mean value (here, $\mathbf{M}\mathbf{x} + \mathbf{k}$) and uncorrelated fluctuations with zero mean value (here, \mathbf{n}). In the following we will always subtract the background from the image, and replace $\mathbf{y} + \mathbf{k}$ with \mathbf{y} for simplicity.

Ideally, the problem of estimating \mathbf{x} given \mathbf{y} should be treated in the maximum likelihood sense with an accurate statistical model for the brightness and the noise [31]. Given the bimodal character of the brightness probability distribution (empty sites have zero brightness and occupied sites have a mean brightness $\mu > 0$), the resulting estimation algorithm would be non-linear, therefore time-consuming, and prone to fall into local minima.

To minimize the computation time and ensure the global convergence of the algorithm, we want to limit ourselves to linear estimators. The optimal linear estimator, also called generalized Wiener filter, is the matrix which minimizes the sum of squared errors between the estimated and true brightnesses:

$$\mathbf{H}_{\text{opt}} \triangleq \arg \min_{\mathbf{H}} [\text{SSE}(\mathbf{H})] , \quad (5)$$

with

$$\text{SSE}(\mathbf{H}) \triangleq \langle \|\hat{\mathbf{x}}(\mathbf{H}) - \mathbf{x}\|_2^2 \rangle , \quad (6)$$

and

$$\hat{\mathbf{x}}(\mathbf{H}) - \langle \mathbf{x} \rangle = \mathbf{H}(\mathbf{y} - \mathbf{M}\langle \mathbf{x} \rangle) . \quad (7)$$

In Eq. (6), \mathbf{x} is treated as a set of random variables, and $\langle \cdot \rangle$ denotes the expectation value over the probability distribution of \mathbf{x} and \mathbf{n} . The optimal estimator therefore provides the best estimates *on average* over all possible experimental outcomes, but not necessarily for all individual outcomes (we will come back to this point later). The reason for removing the expectation value of \mathbf{x} on

both sides of Eq. (7) is to obtain a sparse representation of the estimator, which greatly reduces the computation when dealing with large number of sites.

We show in Appendix A that the solution to Eq. (5) can be written in the form

$$\mathbf{H}_{\text{opt}} = (\mathbf{M}^\top \boldsymbol{\Sigma}_n^{-1} \mathbf{M} + \boldsymbol{\Sigma}_x^{-1})^{-1} \mathbf{M}^\top \boldsymbol{\Sigma}_n^{-1} , \quad (8)$$

where $\boldsymbol{\Sigma}_x \triangleq \langle (\mathbf{x} - \langle \mathbf{x} \rangle)(\mathbf{x} - \langle \mathbf{x} \rangle)^\top \rangle$ is the covariance matrix of the brightness and $\boldsymbol{\Sigma}_n \triangleq \langle \mathbf{n}\mathbf{n}^\top \rangle$ is the covariance matrix of the noise. In the following we will assume that both $\boldsymbol{\Sigma}_x$ and $\boldsymbol{\Sigma}_n$ are diagonal, which means that we neglect inter-site and inter-pixel correlations. It is worth mentioning that the Wiener filter (8) can also be interpreted as the maximum a posteriori (MAP) estimator for a Gaussian prior [31][32], or as the solution of a weighted and regularized least-square problem [33].

In principle, solving the inverse problem of Eq. (7) using Eq. (8) calls for the inversion of the matrix $\mathbf{A} \triangleq \mathbf{M}^\top \boldsymbol{\Sigma}_n^{-1} \mathbf{M} + \boldsymbol{\Sigma}_x^{-1}$. From a computational point of view, it is however much more efficient to solve the equivalent linear system $\mathbf{A}(\hat{\mathbf{x}} - \langle \mathbf{x} \rangle) = \mathbf{b}$, with $\mathbf{b} \triangleq \mathbf{M}^\top \boldsymbol{\Sigma}_n^{-1}(\mathbf{y} - \mathbf{M}\langle \mathbf{x} \rangle)$. Since \mathbf{A} is positive-definite by construction, and sparse because only nearby sites have overlapping PSFs, we naturally choose a sparse conjugate-gradient solver [34] for this task.

IV. TWO-STEP ESTIMATION

The expression (8) of the optimal linear estimator explicitly involves the covariance matrices $\boldsymbol{\Sigma}_x$ and $\boldsymbol{\Sigma}_n$, which are usually not available experimentally. One therefore needs some strategy to infer their value from the measured image itself. We propose to do this in two steps. First, we assume that all sites have the same brightness distribution, and that all pixels have the same noise distribution. We then determine $\langle x \rangle$ from the total number of counts in the image, and treat the ratio Σ_n/Σ_x as a free parameter, which we choose to maximize the Fisher linear discriminant (i.e. the contrast) of the bimodal distribution of estimated brightnesses.

In the second step, we consider that each site has its own occupancy probability, reflecting the prior information contained in the image: the sites which appear brighter in the image are probably occupied, while those which appear darker are probably empty. We introduce the occupancy probability vector \mathbf{p} , and determine \mathbf{p} , μ and σ by maximizing their likelihood given the estimate obtained in the first step. Finally, we compute $\langle \mathbf{x} \rangle$, $\boldsymbol{\Sigma}_x$ and $\boldsymbol{\Sigma}_n$ by applying Eqs. (11) to (13) to each site i , with \mathbf{p} replaced by $(\mathbf{p})_i$. The reader can refer to Appendix B for more details and justifications.

Applying this two-step procedure to the test image displayed in Fig. 1, for instance, we obtain a DER of 1.30 % after the first step and 0.38 % after the second step, compared to 1.91 % with a deconvolution estimator (see below). In the following, we name *globally optimal*

the approach taken in the first step, and *locally optimal* the approach taken in the second step.

V. SIGNAL-TO-NOISE RATIO

A valuable by-product of our approach is the possibility to rigorously define a signal-to-noise ratio for the estimation problem, namely

$$\text{SNR} \triangleq 10 \log_{10} \left(\frac{N_s \mu^2}{\text{SSE}(\mathbf{H}_{\text{opt}})} \right). \quad (9)$$

When the imaging parameters are known, the SNR can be explicitly computed using the following identity, derived in Appendix A:

$$\text{SSE}(\mathbf{H}_{\text{opt}}) = \text{trace}[(\mathbf{I} - \mathbf{H}_{\text{opt}}\mathbf{M})\boldsymbol{\Sigma}_x], \quad (10)$$

where \mathbf{I} is the identity matrix.

As an illustration, let us consider a test image like the one displayed in Fig. 1. Since all sites have the same brightness distribution and all pixels have the same noise distribution, we can write $\langle \mathbf{x} \rangle = \langle x \rangle \mathbf{1}$, $\boldsymbol{\Sigma}_x = \Sigma_x \mathbf{I}$ and $\boldsymbol{\Sigma}_n = \Sigma_n \mathbf{I}$, with

$$\langle x \rangle = p\mu, \quad (11)$$

$$\Sigma_x = p(1-p)\mu^2 + p\sigma^2, \quad (12)$$

$$\Sigma_n = \frac{p\mu}{N_p} (\mathbf{1}^\top \mathbf{M} \mathbf{1}) + k + r^2. \quad (13)$$

With the imaging parameters from Table I, we obtain a SNR of 14.8 dB [35]. As shown in Section VI, the strength of our definition of the SNR is that it synthesizes all system parameters into a single number, which determines the detection error rate. For instance, we obtain almost the same SNR (14.9 dB) if we simultaneously scale up the PSF HWHM from $3a/4$ to a , and multiply both μ and σ by a factor 10, while keeping all other parameters constant. Running our reconstruction method over 50 test images for both sets of imaging parameters, we reach identical detection error rates of $0.2 \pm 0.1\%$ with our locally optimal estimator, compared to about $1.4 \pm 0.1\%$ with a standard deconvolution method (the uncertainty is the standard deviation).

It would be handy of course to have a simpler expression than Eq. (9) to evaluate the SNR, with the individual imaging parameters appearing explicitly. Unfortunately, we can only obtain such expression in the trivial limit where there is no overlap between the PSFs, i.e. $\mathbf{M}^\top \mathbf{M} = \mathbf{I}$. In this case, Eq. (9) reduces to $\text{SNR} \sim 10 \log_{10}[\mu^2(\Sigma_x^{-1} + \Sigma_n^{-1})]$, which means that the signal power is given by the squared brightness mean, and the noise power by (half) the harmonic mean of the brightness and noise variances. We warn the reader, however, that this simple expression must be used very cautiously, as it completely ignores the crucial role played by the PSF overlap. With the parameters of Table I, for instance, it predicts a SNR of about 40 dB, which is 25 dB larger than the correct SNR.

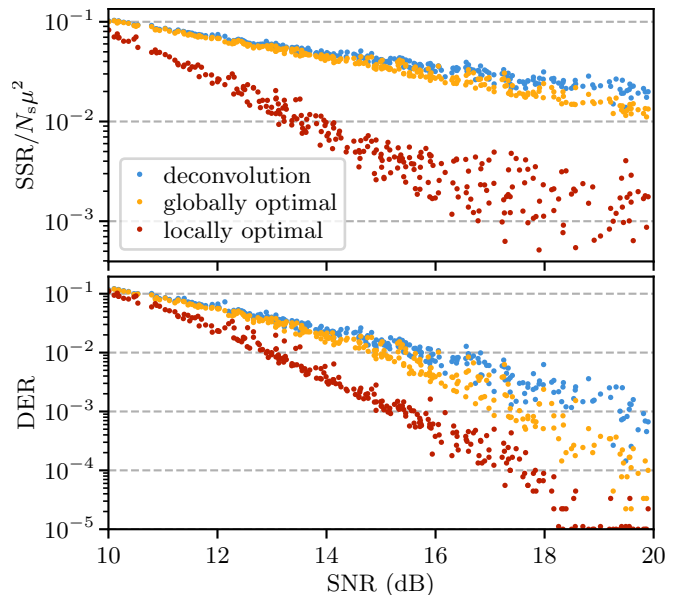


FIG. 2. **Accuracy vs. SNR.** Test images generated with random imaging parameters (given in Table II) are analyzed successively with an estimator based on the Wiener deconvolution filter (blue dots), and with the globally and locally optimal linear estimators (yellow and red dots, respectively). The images are sorted according to their signal-to-noise ratio (SNR, see Eq. (9)). The top panel shows the normalized sum of squared residuals (SSR, see Eq. (2)). The bottom panel shows the detection error rate (DER, see Eq. (3)). A floor value of 10^{-5} was set for the DER so that each point is visible.

number of sites	N_s	300×300	
occupancy probability	p	$[0.2, 0.8]$	
lattice spacing	a	$[1.5, 5]$	pixel
PSF HWHM		$[0.5, 1] \times a$	pixel
brightness mean	μ	$[100, 10\,000]$	count / site
brightness variance	σ^2	$(\mu/10)^2$	count / site
background	k	$[10, 1\,000]$	count / pixel

TABLE II. **Imaging parameters for Fig. 2.** The intervals give the boundaries of the uniform distributions from which the parameters are drawn. The PSF HWHM is defined as a random fraction of the lattice period. The brightness variance is fixed at 10% of the brightness mean. The parameters which do not appear in this table have the same value as in Table I. The brightness variance was set to zero so that the measured detection error rate reflects only the estimator accuracy. We increased the number of sites compared to Table I in order to more measure the DER with a higher precision.

VI. BENCHMARKING

We now compare the performance of the optimal estimator, both in its global and local versions, against a linear estimator based on the popular Wiener deconvolution filter. The implementation of the deconvolution estimator is presented in detail in Appendix C.

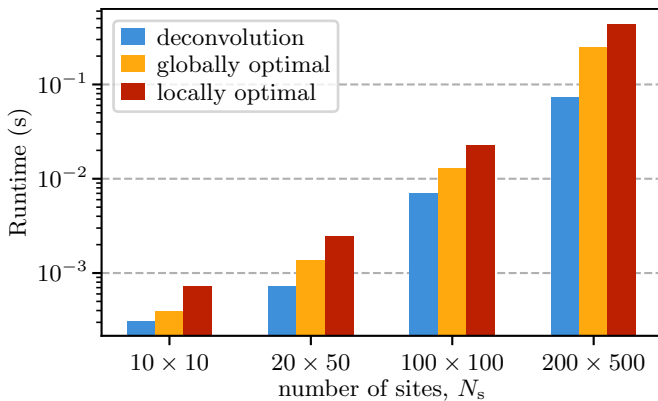


FIG. 3. **Runtime.** The runtime corresponds to the computation of an estimate for an image generated with the imaging parameters in Table I (except for the varying number of sites). It excludes all the steps which precede the computation of the final estimate, like the optimization of the free parameters, or the computation of the matrices \mathbf{M} and $\mathbf{M}^T \mathbf{M}$. The runtime of the locally optimal estimator is the time it takes to run both steps successively, not just the second step. The relative tolerance for the convergence check of the conjugate-gradient solver is set to 10^{-4} .

A. Accuracy

To begin with, we generate hundreds of test images with random imaging parameters, covering a wide range of experimental conditions and SNR, see Table II. We process each image successively with the globally optimal, locally optimal, and deconvolution estimators [36], and compute the estimation and detection accuracies, according to Eqs. (2) and (3). The results are plotted in Fig. 2 as a function of the SNR. We draw two conclusions from these graphs. First, the optimal linear estimator, both in its globally or locally optimal version, systematically outperforms the deconvolution estimator. The gain in accuracy is important with the locally optimal estimator, with a reduction of the DER by a factor ten when the SNR is above 15 dB, i.e. under typical experimental conditions.

Fig. 2 also confirms the relevance of our definition of the SNR as a synthetic indicator of the intrinsic ‘difficulty’ of the estimation problem, since the measured SSR collapse onto a single curve for each estimator. When considering the DER, one can expect that the ratio σ/μ also plays a role as it sets a lower bound on the DER that can be reached at infinite SNR. This effect should however be negligible as soon as σ is a few times smaller than μ .

B. Runtime

Another important aspect to take into consideration when comparing different estimators is their computation time. In Fig. 3, we show the runtimes (wall-clock

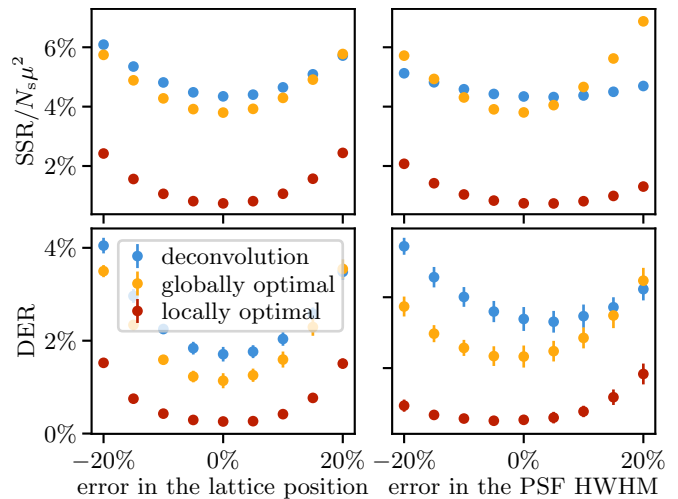


FIG. 4. **Robustness against calibration errors.** Each point is an average over 10 test images generated with the imaging parameters of Table I. The same set of test images was used for each value of the errors in the lattice positions and PSF HWHM. Error bars representing the standard deviation over the test images are drawn for each point, but are sometimes too small to be visible. The errors in the lattice position are given as a percentage of the lattice period a and the errors in the PSF HWHM are given as a percentage of the true value.

times) of the globally optimal, locally optimal, and deconvolution estimators for the imaging parameters in Table I and an increasing number of sites. The runtime of the locally optimal estimator is the time it takes to run both steps of estimation, not just the second step. While the deconvolution method is always faster, the runtime of the optimal estimator remains well below 100 ms for a number of sites as large as 10^4 , which makes it perfectly suitable for real-time usage in all existing experiments.

Here, the numerical implementation is in Python, uses mainly the standard libraries NumPy [37] and SciPy [38], and runs on a standard desktop computer [39]. The runtime is measured using the `%timeit` magic command from IPython, keeping the default settings. The sparse conjugate-gradient solver is a slightly optimized version of the SciPy routine, and includes a Jacobi (or diagonal) preconditioner [40]. It excludes all the steps which precede the computation of the final estimate, like the optimization of the free parameters, or the computation of the matrices \mathbf{M} and $\mathbf{M}^T \mathbf{M}$. We have made this choice because these quantities need not be determined for every single image. Note that the runtime of the deconvolution estimator depends on both N_s and N_p , whereas that of the optimal estimator only depends on N_s .

C. Robustness against calibration errors

All estimators used or proposed so far for the reconstruction of the site occupancy assume that the site co-

ordinates and the PSF have been correctly calibrated beforehand. In this last section, we study how robust the optimal and deconvolution estimators are against two possible calibration errors: an error in the lattice position (or phase) and an error in the PSF HWHM. By error, we mean that the value of the parameter used to build the measurement matrix in Eq. (8) is not equal to the value of the parameter which was used to generate the test image. For a given calibration error, we then computed $\hat{\mathbf{x}}$ using the optimal and deconvolution estimators. The results are displayed in Fig. 4, with the left and right columns showing the effect of an error in the lattice position and in the PSF HWHM, and the top and bottom rows showing the normalized SSR and the DER, respectively. We see that the optimal estimator has a sensitivity to these calibration errors which is comparable to that of the deconvolution estimator, and should therefore perform well under realistic experimental conditions.

VII. CONCLUSION

In conclusion, we have applied the generalized Wiener filter theory to the atom detection in site-resolved fluorescence images of arrays of optical microtraps, and shown that it yields superior results over the standard method based on Wiener deconvolution, while keeping a low computation time, compatible with real-time applications. We expect the same conclusion to hold for any other linear method, including Richardson-Lucy deconvolution, or ordinary least squares [41].

Our method is robust against calibration errors, and offers the possibility (not illustrated in this article) to account for spatial inhomogeneities in the distribution of atoms, readout noise, or PSF. To give just one illustration, one can easily disregard hot pixels by removing the corresponding lines in the measurement matrix. We are therefore convinced that it will keep its accuracy under real experimental conditions.

Benchmarking against supervised or unsupervised machine learning approaches remains to be done. Since our method includes the statistics of the signal and the noise up to the second order moments, it should be competitive with these methods. Of, course, the fact that we can optimize the few free parameters of our estimator from a single image, or just a few images, is a clear asset.

Finally, the Wiener filter theory also lead us to a rigorous definition of a signal-to-noise ratio for the estimation problem. This opens prospect for a more efficient design of future experiments, by taking into account simultaneously the performance of the imaging systems, the expected amount of signal and desired inter-site distance.

ACKNOWLEDGMENTS

The authors also thank Thomas Chalopin and David Clément for their critical reading of the manuscript, and

Anaís Molineri for early work on the problem treated here.

Appendix A: Optimal linear estimator

In this section we explain how we have derived the expression (8) of the optimal linear estimator. We take $\langle \mathbf{x} \rangle = \mathbf{0}$ for simplicity. We start by writing the squared norm as the trace of the outer product and expand all terms:

$$\text{SSE}(\mathbf{H}) = \langle \text{trace}[(\mathbf{H}\mathbf{y} - \mathbf{x})(\mathbf{H}\mathbf{y} - \mathbf{x})^\top] \rangle \quad (\text{A1})$$

$$= \text{trace}[\mathbf{H}\langle \mathbf{y}\mathbf{y}^\top \rangle \mathbf{H}^\top - \mathbf{H}\langle \mathbf{y}\mathbf{x}^\top \rangle - \langle \mathbf{x}\mathbf{y}^\top \rangle \mathbf{H}^\top + \langle \mathbf{x}\mathbf{x}^\top \rangle]. \quad (\text{A2})$$

The optimal estimator is such that the derivative of the SSE with respect to \mathbf{H} is identically zero, which gives [42, Eqs. (100), (104) and (111)]:

$$\left. \frac{d\text{SSE}}{d\mathbf{H}} \right|_{\mathbf{H}_{\text{opt}}} = 2[\mathbf{H}_{\text{opt}}\langle \mathbf{y}\mathbf{y}^\top \rangle - \langle \mathbf{x}\mathbf{y}^\top \rangle] = \mathbf{0}, \quad (\text{A3})$$

hence

$$\mathbf{H}_{\text{opt}} = \langle \mathbf{x}\mathbf{y}^\top \rangle (\langle \mathbf{y}\mathbf{y}^\top \rangle)^{-1}. \quad (\text{A4})$$

We proceed further by replacing the image vector \mathbf{y} with $\mathbf{M}\mathbf{x} + \mathbf{n}$:

$$\langle \mathbf{y}\mathbf{x}^\top \rangle = \langle (\mathbf{M}\mathbf{x} + \mathbf{n})\mathbf{x}^\top \rangle \quad (\text{A5})$$

$$= \mathbf{M}\langle \mathbf{x}\mathbf{x}^\top \rangle, \quad (\text{A6})$$

and

$$\langle \mathbf{y}\mathbf{y}^\top \rangle = \langle (\mathbf{M}\mathbf{x} + \mathbf{n})(\mathbf{M}\mathbf{x} + \mathbf{n})^\top \rangle \quad (\text{A7})$$

$$= \mathbf{M}\langle \mathbf{x}\mathbf{x}^\top \rangle \mathbf{M}^\top + \langle \mathbf{n}\mathbf{n}^\top \rangle, \quad (\text{A8})$$

In deriving these results, we have used the noise properties $\langle \mathbf{x}\mathbf{n}^\top \rangle = \langle \mathbf{x} \rangle \langle \mathbf{n}^\top \rangle$ (\mathbf{x} and \mathbf{n} are uncorrelated), and $\langle \mathbf{n} \rangle = \mathbf{0}$.

The matrices $\langle \mathbf{x}\mathbf{x}^\top \rangle$ and $\langle \mathbf{n}\mathbf{n}^\top \rangle$ are the covariance matrices of \mathbf{x} and \mathbf{n} , denoted $\boldsymbol{\Sigma}_x$ and $\boldsymbol{\Sigma}_n$ in the main text. Combining Eqs. (A4), (A6) and (A8) gives

$$\mathbf{H}_{\text{opt}} = \boldsymbol{\Sigma}_x \mathbf{M}^\top (\mathbf{M} \boldsymbol{\Sigma}_x \mathbf{M}^\top + \boldsymbol{\Sigma}_n)^{-1}. \quad (\text{A9})$$

This expression turns out to be inconvenient for efficiently computing the solution to the problem. We obtain the more useful expression in Eq. (8) by applying the so-called Woodbury identity [42, Eq. (158)] (which holds because $\boldsymbol{\Sigma}_x$ and $\boldsymbol{\Sigma}_n$ are both positive definite by definition).

Finally, we can also compute the SSE corresponding to the optimal estimator by combining Eqs. (A2), (A6), (A8) and (A9):

$$\begin{aligned} \text{SSE}(\mathbf{H}_{\text{opt}}) &= \text{trace}[\mathbf{H}_{\text{opt}}(\mathbf{M}\boldsymbol{\Sigma}_x\mathbf{M}^\top + \boldsymbol{\Sigma}_n)\mathbf{H}_{\text{opt}}^\top \\ &\quad - \mathbf{H}_{\text{opt}}\mathbf{M}\boldsymbol{\Sigma}_x - \boldsymbol{\Sigma}_x\mathbf{M}^\top\mathbf{H}_{\text{opt}}^\top + \boldsymbol{\Sigma}_x] \end{aligned} \quad (\text{A10})$$

$$= \text{trace}[(\mathbf{I} - \mathbf{H}_{\text{opt}}\mathbf{M})\boldsymbol{\Sigma}_x]. \quad (\text{A11})$$

Appendix B: Two-step estimation

The optimal linear estimator depends on the statistical properties of \mathbf{x} and \mathbf{n} through their covariance matrices, Σ_x and Σ_n . It must be applied to a zero-mean image, which requires the knowledge of the expectation value $\langle \mathbf{x} \rangle$. Since these parameters are usually not known before the image is processed, we need a strategy to infer their value from the image itself. This can be done in two steps, which we describe in this section.

1. First step (globally optimal)

In the first step, we write $\langle \mathbf{x} \rangle = \langle x \rangle \mathbf{1}$, $\Sigma_x = \Sigma_x \mathbf{I}$, and $\Sigma_n = \Sigma_n \mathbf{I}$. This means that we assume uniform brightness and noise distributions, and neglect all inter-site or inter-pixel correlations. We can then rewrite the optimal linear estimator in the form

$$\mathbf{H}_{\text{opt}} = \left(\mathbf{M}^\top \mathbf{M} + \frac{\Sigma_n}{\Sigma_x} \mathbf{I} \right)^{-1} \mathbf{M}^\top. \quad (\text{B1})$$

Here, the ratio Σ_n/Σ_x acts as a regularization for the inverse of the Gram matrix $\mathbf{M}^\top \mathbf{M}$. It is of particular importance when the PSF of neighboring sites significantly overlap, and the inverse of the Gram matrix is ill-conditioned.

The mean brightness $\langle x \rangle$ is very easily determined in this case, since it is equal to the sum of all pixel values, divided by the number of sites in the image:

$$\langle x \rangle = \frac{1}{N_s} \sum_i (\mathbf{y})_i. \quad (\text{B2})$$

The regularization parameter Σ_n/Σ_x will be treated as a free parameter, which we call the *regularization parameter*, leading to the parameterized estimator

$$\mathbf{H}(\gamma) = (\mathbf{M}^\top \mathbf{M} + \gamma \mathbf{I})^{-1} \mathbf{M}^\top. \quad (\text{B3})$$

The effect of γ is illustrated in the top panel of Fig. 5. A weak regularization will make the solution extremely sensitive to the noise, leading to a large spread of the estimated brightness distribution. On the contrary, a strong regularization will make the solution insensitive to noise, but will localize it around $\langle x \rangle$. In both cases, the estimate is inaccurate, and the contrast between the two modes of the distribution is weak. On the contrary, the optimal regularization $\gamma_{\text{opt}} \triangleq \Sigma_n/\Sigma_x$ will result in an accurate estimation and a well contrasted distribution. To quantify this behavior, we have applied the parameterized estimator $\mathbf{H}(\gamma)$ to test images generated using the parameters of Table I, and plotted the normalized SSR of the estimates against γ , see the middle panel of Fig. 5. It is clear that the most accurate estimate is obtained for $\gamma = \gamma_{\text{opt}}$.

Of course, one cannot compute the SSR in a real experiment since the true \mathbf{x} is not known. As an alternative,

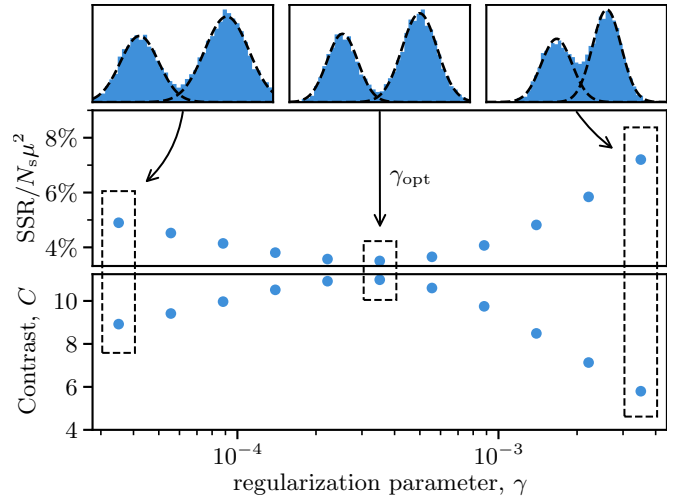


FIG. 5. **Optimization of the regularization parameter in the first step.** The parameterized estimator $\mathbf{H}(\gamma)$ is applied to the test image in Fig. 1. Top panel: estimated brightness distribution for $\gamma = \gamma_{\text{opt}}/10$ (left), $\gamma = \gamma_{\text{opt}}$ (middle), and $\gamma = 10\gamma_{\text{opt}}$ (right), with $\gamma_{\text{opt}} \triangleq \Sigma_n/\Sigma_x$. The dashed lines are the most likely normal distributions associated with each mode of the bimodal distribution. Middle panel: normalized SSR vs. γ . Bottom panel: contrast of the estimated brightness distribution vs. γ .

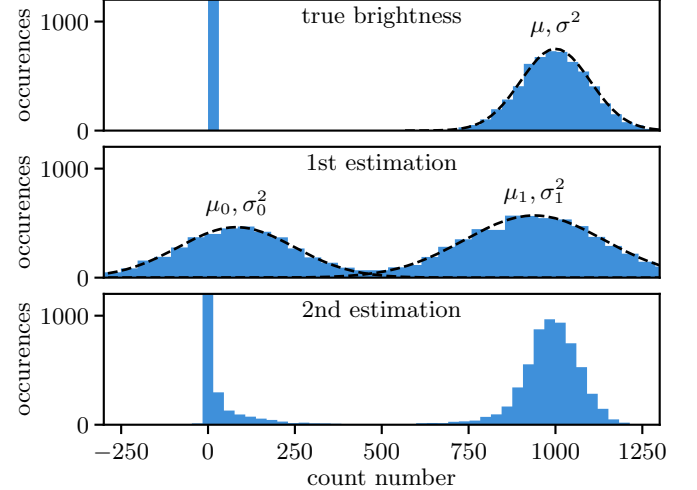


FIG. 6. **Optimal brightness estimate.** Each panel represents a histogram of the brightness (true or estimated) for the test image in Fig. 1. Top panel: true brightness; Middle panel: estimated brightness after the first step; Bottom panel: estimated brightness after the second step. The dashed line in the top panel represents the Gaussian brightness distribution of the occupied sites, whose mean μ and variance σ^2 are given in Table I. The dashed lines in the middle panel represent the two modes of the most likely Gaussian mixture distribution, with means $\mu_{0/1}$ and variances $\sigma_{0/1}^2$.

we propose to optimize γ by maximizing the contrast of the bimodal distribution of $\hat{\mathbf{x}}$. With our idealized test images, the estimate obtained with the parameterized estimator $\mathbf{H}(\gamma)$ obeys a Gaussian mixture distribution,

$$\pi(\hat{\mathbf{x}}) = (1-p)\mathcal{N}(\hat{\mathbf{x}}; \mu_0, \sigma_0) + p\mathcal{N}(\hat{\mathbf{x}}; \mu_1, \sigma_1), \quad (\text{B4})$$

as illustrated for instance in the middle panel of Fig. 6. In Eq. (B4), $\mathcal{N}(x; \mu, \sigma)$ is the normal distribution with mean μ and variance σ^2 evaluated at x , and the labels ‘0’ and ‘1’ refer to the empty and occupied modes, respectively. The parameters p , $\mu_{0/1}$ and $\sigma_{0/1}$ are obtained by maximizing the likelihood function for $\hat{\mathbf{x}}$. A standard definition of the contrast for such distribution is the Fisher linear discriminant:

$$C = \frac{(\mu_1 - \mu_0)^2}{\sigma_1^2 + \sigma_0^2}. \quad (\text{B5})$$

The bottom panel of Fig. 5 shows how this contrast varies with γ . As expected, it reaches a maximum exactly where the SSR reaches a minimum, i.e. for $\gamma = \gamma_{\text{opt}}$.

The optimization procedure described above relies on the fact that the number of sites is large enough to provide a good representation of the distribution of estimated brightnesses. If this is not the case with a single image, it may be necessary to treat simultaneously several images obtained under the same experimental conditions.

2. Second step (locally optimal)

As illustrated in Fig. 2, the estimate obtained in the first step is only slightly more accurate than that obtained with the Wiener deconvolution. We can improve the estimate a lot, however, if we realize that the image contains information on the distribution of site brightnesses that was not used before: the sites which appear brighter in the image are probably occupied, while those which appear darker are probably empty. Following this line of thought means that we now regard the expectation values in Eqs. (6) and (7) as *conditional* on the image.

Let us formalize this idea. We still assume that all occupied sites are characterized by the same brightness mean and variance, denoted μ and σ^2 , but we now allow each site to have its own occupancy probability. These occupancy probabilities are gathered in the vector \mathbf{p} . Within this new model, the covariance matrix of the noise vector is given by

$$\boldsymbol{\Sigma}_n = \text{diag}(\mathbf{H}\mathbf{x} + \mathbf{k} + \mathbf{r}^2), \quad (\text{B6})$$

and the mean value and covariance matrix of the brightness vector by

$$\langle \mathbf{x} \rangle = \mathbf{p}\mu, \quad (\text{B7})$$

$$\boldsymbol{\Sigma}_x = \text{diag}[\mathbf{p}(\mathbf{1} - \mathbf{p})\mu^2 + \mathbf{p}\sigma^2]. \quad (\text{B8})$$

Here, the product between two vectors is element-wise.

To quantify how bright or dark appears in the image, we rely on the $\hat{\mathbf{x}}$ obtained after the first step. We then set the occupancy probability of the i th site to

$$(\mathbf{p})_i = \frac{p\mathcal{N}[(\hat{\mathbf{x}})_i; \mu_1, \sigma_1]}{(1-p)\mathcal{N}[(\hat{\mathbf{x}})_i; \mu_0, \sigma_0] + p\mathcal{N}[(\hat{\mathbf{x}})_i; \mu_1, \sigma_1]}, \quad (\text{B9})$$

where the Gaussian mixture parameters p , $\mu_{0/1}$ and $\sigma_{0/1}$ are those from the first step.

Once we have estimated the occupancy probability vector \mathbf{p} , we can directly apply Eq. (B6) to compute the covariance matrix of the noise vector. For the mean and covariance matrix of the brightness vector, there is one more step to go before applying Eqs. (B7) and (B8), which is to determine the parameters μ and σ^2 . This is done using the identities

$$p\mu = \frac{1}{N_s} \sum_i (\mathbf{y})_i, \quad (\text{B10})$$

and

$$\sigma_1^2 = \sigma^2 + \sigma_0^2. \quad (\text{B11})$$

The first identity corresponds to Eq. (B2), and uses the fact that the optimal linear estimator is unbiased (the mean value is conserved). The second identity expresses the fact that the variance of the brightness in the occupied mode (σ_1^2) combines the variance of the true brightness (σ^2) and the estimation errors, the latter being identified with the variance of the empty mode (σ_0^2) since the brightness of empty sites is identically zero.

In Fig. 6, we compare the distribution of the true brightness for the test image in Fig. 1 with the estimates obtained after each of the two steps described in this section. One sees clearly the effect of associating a different occupancy probability to each site based on the outcome of the first step: it localizes the estimated brightness of the sites around 0 and μ , and strongly reduces the overlap between the two modes. The reason why the second step is so efficient is that all the sites which can be accurately labelled after the first step have their brightness tied to its expected value (0 or μ) at the second step, which effectively reduces the number of parameters to be determined.

Appendix C: Deconvolution estimator

The deconvolution estimator against which we benchmark our optimal linear estimator uses the Wiener deconvolution filter. This filter multiplies each two-dimensional spatial frequency (f_i, f_j) in the image by

$$G(f_i, f_j) = \frac{\tilde{C}(f_i, f_j)}{|\tilde{C}(f_i, f_j)|^2 + \lambda}, \quad (\text{C1})$$

where \tilde{C} is the Fourier transform of the PSF (which is assumed to be uniform across the image), and λ is a free

parameter. The filtered image is then given by

$$\mathbf{y}^* = \mathbf{F}^\dagger \mathbf{G} \mathbf{F} (\mathbf{y} - \bar{\mathbf{y}}), \quad (\text{C2})$$

where \mathbf{F} denotes the unitary Fourier matrix, \mathbf{G} is the diagonal matrix constructed from Eq. (C1), and $\bar{\mathbf{y}} = \bar{y}\mathbf{1}$ is the average of the pixel values in the input image.

To extract the site brightnesses from the filtered image, we first convolve \mathbf{y}^* by a disk-shaped kernel of radius $d \in \mathbb{R}$, i.e. a matrix of size $(2\lceil d \rceil + 1) \times (2\lceil d \rceil + 1)$ such that all pixels within a distance d to the central pixel are equal to 1, and all others to zero. Then, we compute the linear interpolation of the result at the site coordinates.

Since the Wiener deconvolution filter, the convolution, and the linear estimation can all be cast in matrix form, the deconvolution estimator as a whole is a linear estimator.

For each test image, we have performed a joint optimization of the tuning parameters λ and d by maximizing the contrast of the estimated brightness distribution (as defined in Appendix B). Because the process described above is not guaranteed to preserve the absolute brightness of each site, we further applied an affine transformation to the estimated brightness values before computing the SSR for Fig. 2, where the parameters of the affine transformation were optimized to minimize the resulting SSR.

-
- [1] C. Gross and W. S. Bakr, Quantum gas microscopy for single atom and spin detection, *Nature Physics* **17**, 1316 (2021).
- [2] A. M. Kaufman and K.-K. Ni, Quantum science with optical tweezer arrays of ultracold atoms and molecules, *Nature Physics* **17**, 1324 (2021).
- [3] S. M. Kay, *Fundamentals of statistical signal processing, Vol. I: Estimation Theory* (Prentice-Hall, 1993).
- [4] S. M. Kay, *Fundamentals of statistical signal processing, vol. II: Detection theory* (Prentice-Hall, 1998).
- [5] M. Kwon, M. F. Ebert, T. G. Walker, and M. Saffman, Parallel low-loss measurement of multiple atomic qubits, *Physical Review Letters* **119**, 180504.
- [6] M. A. Norcia, A. W. Young, and A. M. Kaufman, Microscopic Control and Detection of Ultracold Strontium in Optical-Tweezer Arrays, *Physical Review X* **8**, 041054 (2018).
- [7] A. Cooper, J. P. Covey, I. S. Madjarov, S. G. Porsev, M. S. Safronova, and M. Endres, Alkaline-Earth Atoms in Optical Tweezers, *Physical Review X* **8**, 041055 (2018).
- [8] I. S. Madjarov, Entangling, controlling, and detecting individual strontium atoms in optical tweezer arrays (2021).
- [9] W. S. Bakr, J. I. Gillen, A. Peng, S. Folling, and M. Greiner, A quantum gas microscope for detecting single atoms in a Hubbard-regime optical lattice, *Nature* **462**, 74 (2009).
- [10] M. F. Parsons, F. Huber, A. Mazurenko, C. S. Chiu, W. Setiawan, K. Wooley-Brown, S. Blatt, and M. Greiner, Site-Resolved Imaging of Fermionic ${}^6\text{Li}$ in an Optical Lattice, *Physical Review Letters* **114**, 213002 (2015).
- [11] A. Omeran, M. Boll, T. A. Hilker, K. Kleinlein, G. Salomon, I. Bloch, and C. Gross, Microscopic Observation of Pauli Blocking in Degenerate Fermionic Lattice Gases, *Physical Review Letters* **115**, 263001 (2015).
- [12] A. Alberti, C. Robens, W. Alt, S. Brakhane, M. Karski, R. Reimann, Artur Widera, and D. Meschede, Super-resolution microscopy of single atoms in optical lattices, *New Journal of Physics* **18**, 053010 (2016).
- [13] J. F. Sherson, C. Weitenberg, M. Endres, M. Cheneau, I. Bloch, and S. Kuhr, Single-atom resolved fluorescence imaging of an atomic Mott insulator, *Nature* **467**, 68 (2010).
- [14] P. Schauss, *High-resolution imaging of ordering in Rydberg many-body systems*, Ph.D. thesis, Ludwig-Maximilians-Universität München (2015).
- [15] M. Miranda, R. Inoue, Y. Okuyama, A. Nakamoto, and M. Kozuma, Site-resolved imaging of ytterbium atoms in a two-dimensional optical lattice, *Physical Review A* **91**, 063414 (2015).
- [16] M. F. Parsons, *Probing the Hubbard Model With Single-Site Resolution*, Ph.D. thesis, Harvard University (2016).
- [17] L. W. Cheuk, *Quantum Gas Microscopy of Strongly Correlated Fermions*, Ph.D. thesis, Massachusetts Institute of Technology (2017).
- [18] R. Yamamoto, H. Ozawa, D. C. Nak, I. Nakamura, and T. Fukuhara, Single-site-resolved imaging of ultracold atoms in a triangular optical lattice, *New Journal of Physics* **22**, 123028 (2020).
- [19] K. Kwon, K. Kim, J. Hur, S. Huh, and J.-y. Choi, Site-resolved imaging of a bosonic Mott insulator of ${}^7\text{Li}$ atoms, *Physical Review A* **105**, 033323 (2022).
- [20] A. La Rooij, C. Ulm, E. Haller, and S. Kuhr, A comparative study of deconvolution techniques for quantum-gas microscope images, *New Journal of Physics* **25**, 083036 (2023).
- [21] J. Mongkolkiattichai, L. Liu, D. Garwood, J. Yang, and P. Schauss, Quantum gas microscopy of fermionic triangular-lattice mott insulators, *Physical Review A* **108**, L061301 (2023).
- [22] S. Buob, J. Höschele, V. Makhalov, A. Rubio-Abadal, and L. Tarruell, A strontium quantum-gas microscope, *PRX Quantum* **5**, 020316 (2024).
- [23] M. Martinez-Dorantes, W. Alt, J. Gallego, S. Ghosh, L. Ratschbacher, Y. Völzke, and D. Meschede, Fast non-destructive parallel readout of neutral atom registers in optical potentials, *Physical Review Letters* **119**, 180503 (2017).
- [24] A. H. Burrell, D. J. Szwer, S. C. Webster, and D. M. Lucas, Scalable simultaneous multiqubit readout with 99.99% single-shot fidelity, *Physical Review A* **81**, 040302 (2010).
- [25] L. R. B. Picard, M. J. Mark, F. Ferlaino, and R. v. Bijnen, Deep learning-assisted classification of site-resolved quantum gas microscope images, *Measurement Science and Technology* **31**, 025201 (2019).
- [26] J. Verstraten, K. Dai, M. Dixmieras, B. Peaudecerf,

- T. d. Jongh, and T. Yefsah, In-situ imaging of a single-atom wave packet in continuous space, arXiv:2404.05699 [quant-ph].
- [27] A. Impertro, J. F. Wienand, S. Häfele, H. von Raven, S. Hubele, T. Klostermann, C. R. Cabrera, I. Bloch, and M. Aidelsburger, An unsupervised deep learning algorithm for single-site reconstruction in quantum gas microscopes, *Communications Physics* **6**, 1 (2023).
- [28] J. Winklmann, A. Alberti, and M. Schulz, Comparison of atom detection algorithms for neutral atom quantum computing, in *2024 IEEE International Conference on Quantum Computing and Engineering (QCE)*, Vol. 01 (2024) pp. 1048–1057.
- [29] See Supplemental Material.
- [30] More elaborate models exist, such as the one recently proposed in [43]. These models are useful to simulate a specific experimental setup, less so to provide ‘prototypical’ test images.
- [31] G. Demoment and Y. Goussard, Inversion within the probabilistic framework, in *Bayesian Approach to Inverse Problems* (John Wiley & Sons, Ltd, 2008) Chap. 3, pp. 59–78.
- [32] Since our optimal linear operator involves only the first two moments of the signal and of the noise, it exhausts all the available information when these variables are normally distributed (which is not the case here, in particular given the bimodal distribution of \mathbf{x}). It is therefore not a surprise that it can also be considered optimal in the Bayesian sense in this case. We stress, however, that it remains optimal in the weaker sense of Eqs. (5) and (6) for arbitrary signal and noise distributions.
- [33] The weighted and regularized least-square problem amounts to minimizing the objective function of the form $f(\mathbf{x}) = (\mathbf{y} - \mathbf{M}\mathbf{x})^T \mathbf{W}(\mathbf{y} - \mathbf{M}\mathbf{x}) + \mathbf{x}^T \mathbf{R}\mathbf{x}$. The role of the regularization matrix \mathbf{R} (here identified with $\Sigma_{\mathbf{x}}^{-1}$) is to improve the stability of the estimate when the standard least-square estimator $(\mathbf{M}^T \mathbf{W} \mathbf{M})^{-1} \mathbf{M}^T \mathbf{W}$ is ill-conditioned. In our context, this happens when the PSFs of neighboring sites significantly overlap. The regularization therefore plays a crucial role in the context of optical lattices, less so in the context of optical tweezer arrays.
- [34] Such solver is available in all standard scientific computing library. In Python one may use the `sparse.linalg.cg` routine from the SciPy library [38].
- [35] The SNR is computed for a patch of 30×30 sites (rather than over the full image) to reduce the computation time of the inverse matrix in Eq. (8).
- [36] The globally and locally optimal estimates in Fig. 2 were obtained using the true imaging parameters because the wide range of imaging parameters covered by the dataset, which includes very difficult situations, makes the fully unsupervised procedure described in Appendix B less reliable.
- [37] C. R. Harris, K. J. Millman, S. J. van der Walt, R. Gommers, P. Virtanen, D. Cournapeau, E. Wieser, J. Taylor, S. Berg, N. J. Smith, R. Kern, M. Picus, S. Hoyer, M. H. van Kerkwijk, M. Brett, A. Haldane, J. F. del Río, M. Wiebe, P. Peterson, P. Gérard-Marchant, K. Sheppard, T. Reddy, W. Weckesser, H. Abbasi, C. Gohlke, and T. E. Oliphant, Array programming with NumPy, *Nature* **585**, 357 (2020).
- [38] P. Virtanen, R. Gommers, T. E. Oliphant, M. Haberland, T. Reddy, D. Cournapeau, E. Burovski, P. Peterson, W. Weckesser, J. Bright, S. J. van der Walt, M. Brett, J. Wilson, K. J. Millman, N. Mayorov, A. R. J. Nelson, E. Jones, R. Kern, E. Larson, C. J. Carey, Í. Polat, Y. Feng, E. W. Moore, J. VanderPlas, D. Laxalde, J. Perktold, R. Cimrman, I. Henriksen, E. A. Quintero, C. R. Harris, A. M. Archibald, A. H. Ribeiro, F. Pedregosa, P. van Mulbregt, and SciPy 1.0 Contributors, SciPy 1.0: Fundamental Algorithms for Scientific Computing in Python, *Nature Methods* **17**, 261 (2020).
- [39] Intel Core i9-10900K CPU with the Intel MKL library.
- [40] Source code available as Supplemental Material.
- [41] The ordinary least squares estimator, $\mathbf{H}_{\text{OLS}} = (\mathbf{M}^T \mathbf{M})^{-1} \mathbf{M}^T$, is ill-conditioned when the PSFs have a significant overlap, meaning that its output is exaggeratedly sensitive to the noise in the image.
- [42] K. B. Petersen and M. S. Pedersen, *The matrix cookbook* (2012), version 20121115.
- [43] J. Winklmann, D. Tsevas, and M. Schulz, Realistic neutral atom image simulation, in *2023 IEEE International Conference on Quantum Computing and Engineering (QCE)*, Vol. 01 (2023) pp. 1349–1359.